

# Numerical investigation of turbulent flame-vortex interaction in premixed cavity stabilized flames

Cal J. Rising<sup>a,\*</sup>, Gabriel B. Goodwin<sup>a</sup>, Ryan F. Johnson<sup>a</sup>, David A. Kessler<sup>a</sup>, Jonathan Sosa<sup>a</sup>, Mason Thornton<sup>b</sup>, Kareem A. Ahmed<sup>b</sup>

<sup>a</sup> Naval Research Laboratory, 4555 Overlook Ave. SW, Washington, 20375, DC, USA

<sup>b</sup> Mechanical and Aerospace Engineering, University of Central Florida, 12670 Pegasus Blvd., Orlando, 32816, FL, USA

## ARTICLE INFO

### Article history:

Received 15 March 2022

Received in revised form 16 June 2022

Accepted 6 August 2022

Available online 12 August 2022

Communicated by Y. Yanxing

### Keywords:

Turbulent combustion  
Flame-vortex interaction  
Premixed combustion  
Cavity stabilized flames  
Numerical simulations

## ABSTRACT

The combustion dynamics of a mixture of ethylene and air in a cavity flameholder are examined using high-resolution numerical simulations. The simulations are performed using both laminar and turbulent inflow boundary conditions to characterize the effects freestream turbulence on the flame-vortex interactions within the combustor. Experimental test results are utilized to validate the simulation's ability to capture the relevant flow and flame behavior. The turbulence intensity is shown to influence the structure of the flow field by creating a more dominant primary vortex within the combustor and decreasing the shear layer reattachment length. The integral length scales and energy spectra are calculated throughout the domain and show that the flow is driven by smaller turbulent eddies within the ramp region of the combustor. The flame-vortex interaction is further examined and revealed to cause an instability forming in the combustor under both laminar and turbulent conditions. The instability is confirmed by examining the pressure fluctuations within the combustor and it is demonstrated that the time scale of the pressure fluctuations corresponds to the frequency of the vortex shedding from the ramp wall.

Published by Elsevier Masson SAS.

## 1. Introduction

Hydrocarbon-fueled dual-mode scramjets have begun to be extensively studied as researchers aim to utilize vehicles which can operate across a variety of flight speeds. The operating conditions within ramjet and scramjet mode are distinct and still need to be explored fully. In order to combat the challenges associated with operating at these conditions, a cavity flameholder has been commonly implemented due to the low-speed recirculation zone created allowing for the flame to be stabilized in the shear layer [1]. Additionally, cavity flameholders are advantageous due to their low pressure loss and drag generation [2]. Operating across a spectrum of flight speeds can result in variable freestream turbulence conditions which can consequently impact the flame and flow field interactions requiring a thorough understanding of the combustion dynamics occurring within the cavity.

Cavity flameholder stability results from low temperature reactants being entrained into the high temperature product region within the recirculation zone. Reactant entrainment occurs in two regions, the cavity shear layer and the cavity aft wall where the shear layer reattaches [3]. Previous research performed by Huellmantel et al. examined the impacts of inflow velocity and cavity geometry to determine blowout limits for subsonic flames [4]. While this research provided insights into the flame stability as function of velocity, the influence of incoming turbulence was not fully explored. Research regarding the impact of augmented freestream turbulence has primarily been performed on bluff-body and backward-facing step flameholders. Previous research on bluff-body flameholders has indicated that altering freestream conditions have a significant impact on the shear layer and recirculation zone [5–7]. For example, Massey et al. indicated that there is a decrease in recirculation zone lengths and shear layer thickness under increasing turbulent conditions [8]. Much of the prior work on backward-facing step configurations has focused on altering thermochemical properties (e.g. fuel composition, equivalence ratio) and determined that the heat release of combustion results in decreased recirculation zone lengths [9–11].

The formation of vortical structures from any flameholding device and their subsequent interaction with the flame introduces

\* Corresponding author.

E-mail addresses: cal.rising@nrl.navy.mil (C.J. Rising), gabe.goodwin@nrl.navy.mil (G.B. Goodwin), ryan.johnson@nrl.navy.mil (R.F. Johnson), david.kessler@nrl.navy.mil (D.A. Kessler), jonathan.sosa@nrl.navy.mil (J. Sosa), thorntonmason@knights.ucf.edu (M. Thornton), kareem.ahmed@ucf.edu (K.A. Ahmed).

unsteadiness, curvature, and straining to the flame-front [12–14]. These interactions have been studied extensively in backward-facing step configurations and shown to result in unstable operating conditions [15–18]. The unsteady interaction between the flame and vortices, formed as a result of the flow separation, cause significant oscillations in the heat release and pressure within the combustor [13,19]. These studies have primarily focused on altering the thermochemical properties (e.g. freestream temperature, equivalence ratio) and not on altering the inflow turbulence intensity to quantify the implications on operating stability. While the flow field characteristics are similar between a cavity and backward-facing step, altering the aft wall geometry and its implications on the flame-vortex interaction and operating stability warrant further study.

Prior research has highlighted the direct connection between turbulent flow field statistics and flame scales. This is commonly identified utilizing the Karlovitz number ( $Ka$ ), which is defined as the ratio of chemical time scales to turbulent time scales or  $Ka = (l_f/L_x)^{1/2}(u'/S_L)^{3/2}$ , where  $l_f$  is the laminar flame thickness,  $L_x$  is the integral length scale,  $u'$  is the turbulent velocity fluctuations, and  $S_L$  is the laminar flame speed [20]. Prior direct numerical simulations have explored turbulent flames subjected to a wide variety of  $Ka$  (<1 to >100) and have demonstrated the impact of turbulence on the flame [21–25]. It has been shown that with low turbulence conditions (low  $Ka$ ), flames are influenced by the large scale turbulent eddies resulting in wrinkling and accelerated propagation velocity [26,27]. As turbulence is increased there is a corresponding increase in the small scale eddies within the flow which can penetrate the flame thickness, resulting in smaller scale wrinkling and broadening of the preheat layer [24]. The interdependence between turbulence and combustion indicates a need for the relevant flame and flow scales throughout the reaction domain to be explored.

The current work examines two and three-dimensional simulations of the University of Central Florida Propulsion and Energy Research Laboratory's cavity stabilized combustion facility to explore the influence of freestream turbulence on the dynamics of the flame and flow field. Experimental results are used to validate the simulation behavior using average statistics. Large Eddy Simulations (LES) are performed using the Naval Research Laboratory's JENRE<sup>®</sup> Multiphysics Framework with a three step, seven species global chemical mechanism for ethylene-air combustion. The results focus on exploring the impact turbulence has on relevant flow quantities such as the shear layer reattachment length, recirculation zone length, and turbulent flow quantities (integral length scales, energy spectra) to determine how these correspondingly influence the flame stability and dynamics within the cavity. The turbulent statistics reveal a shift from a flow field driven by large scale vortex structures in the cavity towards a more turbulent, small scale vortex structure-dominated flow at the cavity aft wall. Due to the change in the flow-field, instabilities generated by flame-vortex interactions are examined to determine the influence of freestream turbulence on the flame behavior by investigating the pressure fluctuations and vortex shedding behavior within the cavity.

## 2. Numerical methodology

### 2.1. Governing equations and approach

In this study, a fully conservative formulation of the multi-component, chemically reacting Navier Stokes equations [28] are solved, which are defined as

$$\frac{\partial \rho \mathbf{v}}{\partial t} + \nabla \cdot (\rho \mathbf{v} \otimes \mathbf{v} + p \mathbb{I}) = \nabla \cdot \boldsymbol{\tau}, \quad (1)$$

$$\frac{\partial (\rho e_t)}{\partial t} + \nabla \cdot ((\rho e_t + p) \mathbf{v}) = \nabla \cdot \left( \lambda \nabla T - \sum_{i=1}^{N_s} W_i C_i h_i \mathbf{V}_i + \boldsymbol{\tau} \cdot \mathbf{v} \right), \quad (2)$$

$$\frac{\partial C_i}{\partial t} + \nabla \cdot (C_i (\mathbf{v} + \mathbf{V}_i)) = \omega_i \text{ for } i = 1 \dots N_s, \quad (3)$$

where  $\rho$  is density,  $\mathbf{v}$  is velocity,  $p$  is pressure,  $\mathbb{I}$  is an identity matrix,  $\boldsymbol{\tau}$  is the deviatoric stress tensor as defined in Eq. (2.17) in [28],  $e_t$  is total energy,  $\lambda$  is conductivity,  $T$  is temperature,  $N_s$  is the number of species,  $W_i$  is molecular weight,  $C_i$  is concentration,  $h_i$  is enthalpy,  $\mathbf{V}_i$  is diffusion velocity,  $\omega_i$  is the production source term, and subscript  $i$  indicates species  $i$ . The production source term is calculated from the progress reaction rates for any number of reactions and reaction types. Pressure is determined using the equation of state,

$$p = R^0 T \sum_{i=1}^{N_s} C_i, \quad (4)$$

where  $R^0$  is the universal gas constant. The species diffusion velocity is defined by

$$\mathbf{V}_i = \frac{D_i}{C_i} \nabla C_i - \frac{D_i}{\rho} \nabla \rho, \quad (5)$$

where  $D_i$  is the mixture-averaged diffusion coefficient. All transport coefficients are calculated using mixture-averaged approaches, full details of the approach can be found in Johnson and Kercher [28]. It was previously demonstrated that no artificial viscosity, stabilization, or filtering methods are required to stabilize the multi-component, chemically reacting flows simulated in this work [28].

The total energy, in this model, is defined as

$$\rho e = \rho u + \frac{1}{2} \rho \mathbf{v} \cdot \mathbf{v}, \quad (6)$$

where  $e$  is the total energy. Internal energy can be defined as a function of total enthalpy,  $\rho u = \rho h_t - p$ , where  $h_t$  is total enthalpy and  $\rho h_t = \sum_{i=1}^{N_s} W_i C_i h_i$ , where  $h_i$  is a nonlinear function with respect to temperature.

Equations (1)–(3) are discretized using the DG method. The resulting DG space semi-discretization, Eq. (3.6) of [28], is integrated temporally with a second order strong-stability-preserving Runge-Kutta method [29]. The temporal integration of the source term is separated from the temporal integration of the conservation laws via Strang operator splitting. The resulting system of ordinary differential equations, describing the influence of the source term on the temporal evolution of the state, is integrated using DGODE [28]. For  $\omega_i$ , a three step, seven species chemical mechanism is used to model the ethylene-air combustion using the reaction rates developed for prior cavity stabilized flame simulations by Peterson and Hassan et al. [30,31]. The included chemical reactions and values used to calculate the reaction rates are provided in Table 1. This global mechanism, which has been calibrated to reproduce flame speed across a range of conditions, is selected because it has been shown to have comparable results to a more detailed chemical model with significantly reduced computational expense [31].

### 2.2. Computational geometry and boundary conditions

Two and three-dimensional simulations are performed on the cavity stabilized flame facility shown in Fig. 1. The domain consists of a 15 mm height channel which leads premixed fuel and air into the cavity flame stabilizer. The step height ( $H$ ) is 16 mm

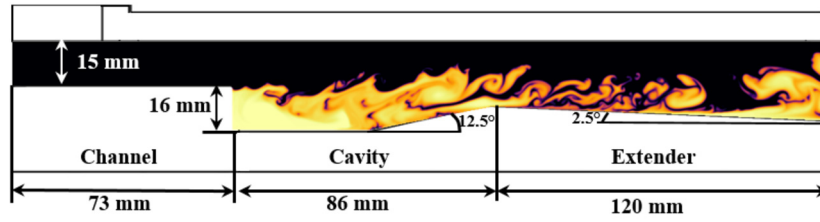


Fig. 1. Computational domain of cavity stabilized flame facility.

Table 1

Three-step global flamespeed mechanism from Peterson [31].

Reaction	A ((m <sup>3</sup> /kmol) <sup>n-1</sup> /s)	b	T <sub>a</sub> (K)
C <sub>2</sub> H <sub>4</sub> + O <sub>2</sub> ⇌ 2CO + 2H <sub>2</sub>	2.23E+11	2.09	15900
2CO + O <sub>2</sub> ⇌ 2CO <sub>2</sub>	3.64E+8	1.86	9870
2H <sub>2</sub> + O <sub>2</sub> ⇌ 2H <sub>2</sub> O	2.55E+17	-0.77	3.6

and the aft wall of the cavity is angled at 12.5°. The inflection point of the ramp is determined based on a relief angle of 2.5° which continues for the length of the extender section. The three-dimensional simulation is completed by extending the geometry 10 mm in the z-direction. The domain is initially filled with a stoichiometric fuel and air mixture at 1 atm and 300 K. The flow is ignited after several flow through residence times by initializing a high temperature circular region in the cavity. The simulations are performed with turbulent and laminar inflow boundary conditions and the walls are no slip. The inflow boundary conditions will be discussed in more detail in Section 2.3. The plenum to which the combustor exhausts to is not depicted in Fig. 1, however it consists of an additional 200 mm of length which exhausts to atmospheric conditions. This additional length is utilized to minimize the influence of the subsonic, characteristic outflow boundary condition on the flow within the combustor.

The mesh utilized in the simulations consisted of 200 μm second order accurate DG(*p* = 1) triangular elements throughout the combustor. This resulted in a total of 397 K elements in the mesh. Estimations were performed to approximate the Kolmogorov scales under laminar and turbulent inflow conditions utilizing Kolmogorov's similarity hypothesis [32]. The Kolmogorov scales for the turbulent inflow boundary condition are presented in Fig. 2. The same procedure is taken for the laminar inflow condition and an average value is extracted from the channel region near the cavity lip. The Kolmogorov scales are 250 μm and 65 μm within the channel region for the laminar and turbulent inflow boundary conditions. However, the Kolmogorov scales within the cavity experience an increase in magnitude indicating that the mesh adequately resolves these scales within the flameholder. Results will be presented utilizing third order accurate DG(*p* = 2) elements to demonstrate that the accuracy of the DG(*p* = 1) elements is sufficient to resolve the flame structure and flow field metrics.

### 2.3. Inflow conditions

Laminar and turbulent inflow boundary conditions are used to isolate the impacts of altering the freestream turbulence on the flame and flow interactions. The nomenclature laminar and turbulent is used to differentiate between inlet velocity profiles which are either unperturbed (laminar) or perturbed (turbulent). For each inflow condition an equivalence ratio of  $\phi = 1.0$  is selected. The laminar condition utilizes a characteristic, subsonic inlet boundary condition with  $V_0 = 100$  m/s. The inflow utilizing this boundary condition is unperturbed, although velocity fluctuations in the channel, prior to the cavity, are generated from the boundary layer and pressure waves. In order to achieve higher turbulent inflow

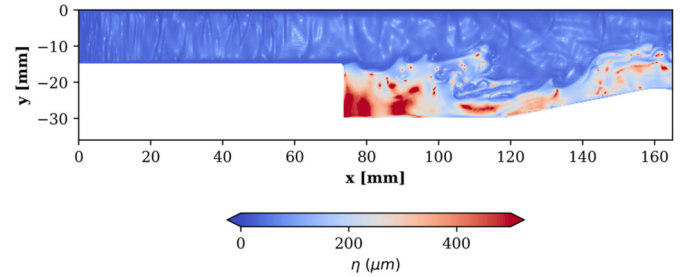


Fig. 2. Calculated Kolmogorov scales for turbulent inflow conditions. (For interpretation of the colors in the figure(s), the reader is referred to the web version of this article.)

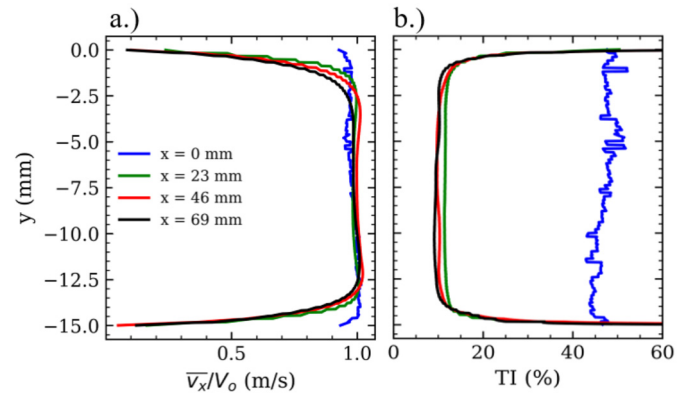


Fig. 3. a.) Average streamwise velocity profiles and b.) Turbulence intensity along the channel for the turbulent inflow boundary condition.

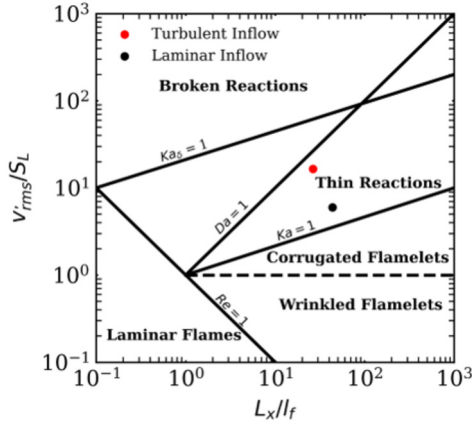
conditions a method to synthetically generate turbulence at the inflow boundary developed by Davidson et al. was selected [33]. This boundary condition generates temporally and spatially correlated turbulent velocity fluctuations about a prescribed mean velocity profile by decomposing the turbulent signal into discrete Fourier modes. The fluctuations are calculated based on a von Karman spectrum over a finite region of wavenumber space which has been discretized into set number of nodes. To ensure temporal correlation in the velocity fluctuations, an asymmetric time filter is applied. This method has been successfully implemented in previous reacting turbulent flow simulations [34–36]. Using this forced turbulence boundary condition a high turbulence intensity is applied at the inflow which decays along the length of the channel. The turbulence intensity reaches a steady value of 10% based on  $V_0 = 100$  m/s prior to reaching the cavity lip. The intensity of 10% is targeted based on previous LES studies of premixed ethylene-air cavity-stabilized flames [37,38]. The average streamwise velocity profiles and turbulence intensity taken at locations along the length of the channel for the turbulent inflow boundary condition are presented in Fig. 3.

For each inflow boundary condition the relevant flow and flame scales are provided in Table 2. Table 2 consists of the integral length scales ( $L_x$ ), the bulk turbulent velocity fluctuations ( $v'_{rms}$ ),

**Table 2**

Laminar and turbulent inflow simulation test conditions.

Condition	$V_o$ (m/s)	$v'_{rms}$ (m/s)	$L_x$ (mm)	$S_L$ (m/s)	$l_f$ (mm)	$\eta$ ( $\mu$ m)	$Ka$
Laminar Inflow	100	3	13	0.66	0.302	250	1.45
Turbulent Inflow	100	10	7	0.66	0.302	65	12.98

**Fig. 4.** Test points on turbulent premixed flame diagram.

the laminar flame thickness ( $l_f$ ), the laminar flame speed ( $S_L$ ), the Kolmogorov scales ( $\eta$ ), and the Karlovitz number ( $Ka$ ). The integral length scales are defined as the two point autocorrelation of the fluctuating velocity, which is given by

$$L_i = \int_0^\infty \frac{\overline{v'_i(x, y)v'_i(x, y+r)}}{\overline{v'_i(x, y)^2}} dy \quad (7)$$

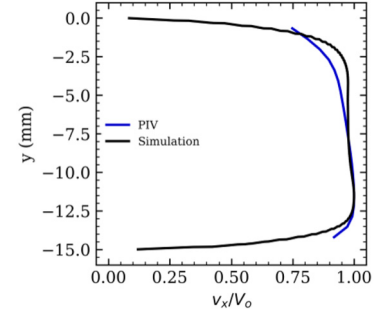
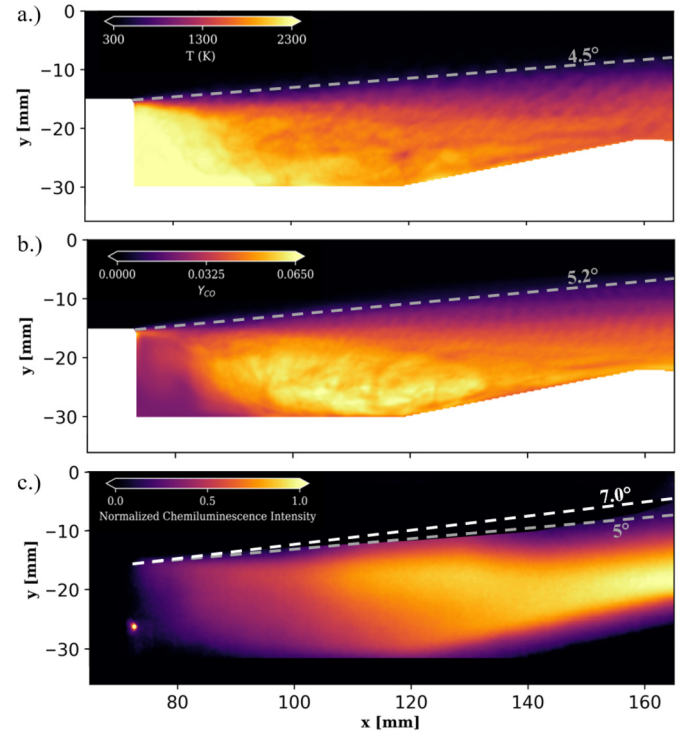
where  $i$  represents the direction,  $L_i$  is the integral length scale, and  $v'_i$  is the local velocity component fluctuation [39]. This method is utilized to calculate the length scales at the cavity lip and downstream for both inflow boundary conditions. The integral length scales and turbulent velocity fluctuations provided in Table 2 are extracted at the cavity lip to capture the incoming turbulent flow statistics prior to interacting with the flame. The laminar flame speed and thickness are taken from literature which explored stoichiometric ethylene-air flames under similar temperature and pressure conditions [40]. These quantities are used to plot the current test conditions on the Borghi Diagram in Fig. 4 and reveal that each test case lies within the thin reaction regime.

### 3. Results

#### 3.1. Two-dimensional simulations

##### 3.1.1. Experimental validation

Experimental results from the University of Central Florida are first used to compare and validate the simulation results using average statistics. The experimental facility consists of the geometry shown in Fig. 1, in a  $127 \times 45$  mm optically accessible test section. The ethylene and air is introduced upstream in a 1.5 m long,  $130 \times 155$  mm rectangular plenum to allow adequate time for mixing. Turbulence is introduced into the facility by including a mesh grid upstream of the test section to perturb the flow. A spark plug in the center of the cavity floor is used to ignite the flow. Further details on the experimental facility flow control are available in previous literature, with the only difference being the bluff-body removed and the test section includes the cavity geometry presented in Fig. 1 in the test section [41,42]. In the experimental facility, particle image velocimetry (PIV) measurements are captured at 20 kHz in the channel region prior to the cavity to measure

**Fig. 5.** Velocity profiles taken at cavity lip ( $x = 69$  mm) for turbulent inflow from experiment and simulation.**Fig. 6.** Flame angle from time averaged a.) simulation temperature measurements b.) simulation CO mass fraction c.) experimental chemiluminescence measurements.

the incoming bulk velocity under turbulent inflow conditions. The channel velocity profiles from the experiment and turbulent inflow simulation are presented within Fig. 5. The velocity profiles demonstrate that the simulations are in good agreement with the experimental results.

Additionally, to confirm the corresponding flame behavior is suitably captured by the simulation, a comparison of the flame angle is made with 20 kHz broadband chemiluminescence measurements for the turbulent inflow case. The flame angle from experimental measurements and the simulations are depicted in Fig. 6. Since a global mechanism with a limited number of species and reactions is used, there is not a specific species which can be used to directly compare the flame angle to the experimental chemiluminescence measurements. Therefore, the time averaged temperature and mass fraction of CO are presented in Fig. 6 as



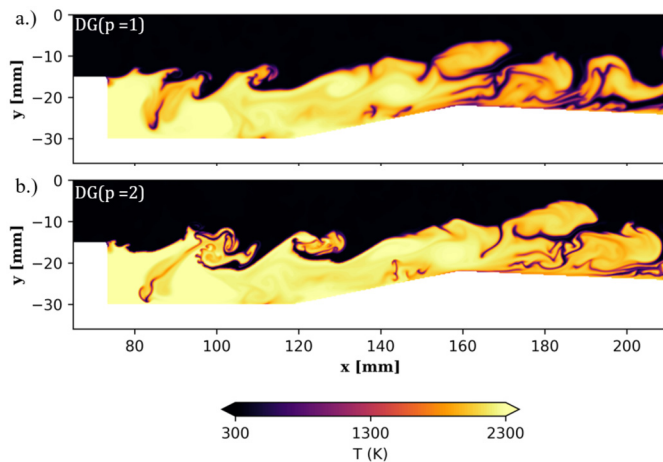


Fig. 7. Instantaneous temperature contour for a.) DG( $p = 1$ ) elements b.) DG( $p = 2$ ) elements.

they are indicative of the reaction progress. The simulation flame angle is approximately  $4.5^\circ$  and  $5.2^\circ$  when measured from the temperature and CO mass fraction, respectively, while the experimental angle is approximately  $5^\circ$ . The white dashed line in Fig. 6b represents the theoretical calculation of  $7.1^\circ$  based on the turbulent flame speed correlation of Peters considering a turbulence intensity of 10% and it is noted that the simulation underpredicts the theoretical angle calculation [43]. The general agreement between flame shape provides confidence that the turbulent inflow boundary condition is capable of capturing the turbulent dynamics influencing the flame.

### 3.1.2. Higher order simulation

To confirm the resolution is suitable to examine the results on an instantaneous basis a higher order simulation utilizing third order accurate DG( $p = 2$ ) elements is completed. This increase in accuracy, however, does result in an increase in computational expense. The flame and flow field are examined for both elements to determine the impact of the increased resolution. Instantaneous temperature contours of the cavity are presented in Fig. 7. The contours indicate that the flame remains attached at the cavity lip, with the primary difference lying in the finer detail of the small scale wrinkling of the flame front. The global structure of the flame is similar and there is minimal change in the flame angle. To examine the impacts of the DG( $p = 2$ ) elements more quantitatively, probability density functions (PDF) of the vorticity within the cavity and ramp are extracted and compared. The PDF's are presented in Fig. 8 and reveal that there is minimal difference in the distribution of vorticity in both the cavity and ramp. This demonstrates that the resolution of the DG( $p = 1$ ) element simulation is suitable for capturing the flame behavior and providing accurate first order statistics such as vorticity.

### 3.1.3. Average flow field

As a general overview, the time-averaged flow fields are first examined to gain insight into the flame and flow behavior. In Fig. 9 the average vorticity ( $\omega_z$ ) with streamlines overlaid is shown for nonreacting and reacting conditions. The gray dashed lines in Fig. 9 represent the  $v_x = 0$  m/s streamline to indicate where the shear layer reattaches on the aft ramp wall. Comparing non-reacting and reacting conditions reveals that combustion heat release results in a thinner shear layer, leading to a larger secondary vortex forming within the cavity. The nonreacting shear layer also reattaches further downstream on the ramp, resulting in the primary vortex dominating the vorticity dynamics within the cavity. However, under reacting conditions the shear layer reattaches earlier on the

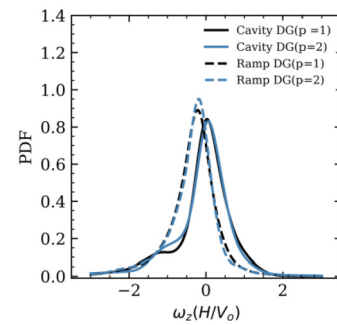
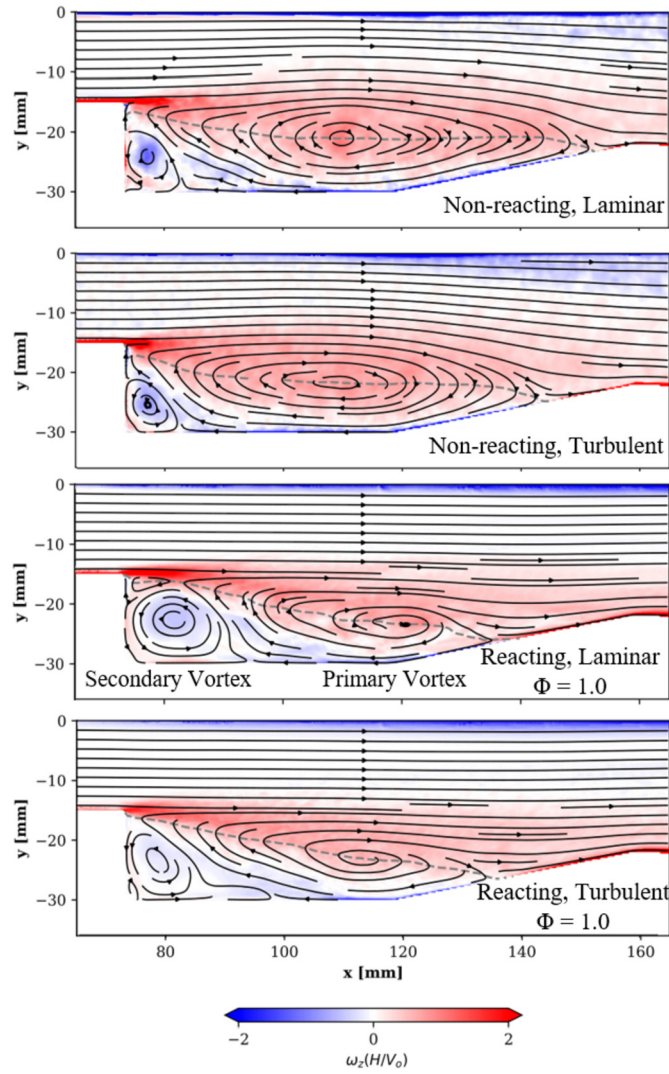


Fig. 8. PDF's of instantaneous vorticity extracted from the cavity and ramp for DG( $p = 1$ ) elements and DG( $p = 2$ ) elements.

ramp. The secondary vortex results in the pooling of hot combustion products near the wall which allows for continuous ignition of the flame in the cavity shear layer.

Similarly the influence of the turbulence can be identified as an increase in freestream velocity fluctuations, results in a shorter shear layer reattachment length, which is consistent with previous studies utilizing different flameholders [9,10]. This coupled with the effects of combustion heat release result in the reattachment length diminishing further. It is also worth noting that the size of the secondary vortex decreases by approximately half the size under reacting turbulent inflow conditions. Previous research by Hong et al. indicated that as the size of the secondary eddy is diminished, the combustor becomes more influenced by thermoacoustic instabilities [11]. This study utilized altering equivalence ratios to alter the vortex dynamics within the flameholder, however, the results presented in Fig. 9 indicate that turbulence intensity has a similar influence on the flow-field within a cavity while holding the thermochemical properties constant. Instabilities within the combustor will be further examined using instantaneous results in Section 3.1.4

As previously noted there are two features contributing to vorticity generation within the flow field which can augment the turbulent statistics, the shear layer and aft wall reattachment zone. Understanding the integral length scales throughout the combustor can help identify the type of flame-vortex interactions which occur there. The integral length scales  $L_x$  and  $L_y$  at discrete locations are presented in Fig. 10 for the reacting laminar and turbulent inflow boundary conditions. The length scales are calculated at each  $y$ -coordinate from  $y = 0$  mm to the minimum  $y$ -dimension at each  $x$  location. The profiles are then averaged to determine the singular value presented in Fig. 10. The length scales are further separated by examining the values in the reactant and product region to identify the impacts of the combustion process, which was previously shown in Fig. 2 to increase size of the Kolmogorov scales experienced in the flow field. The reactant and product region for average results are determined using the flame angle presented in Fig. 6. The length scales for the reactant laminar inflow condition begin on the order of the channel size until they reach the cavity and undergo an increase in  $L_y$  as a result of the large eddies shed from the cavity lip. As these large eddies dissipate downstream the integral length scales correspondingly decrease. In contrast under the turbulent inflow condition the reactant integral length scales remain nominally constant throughout the domain. There is a slight increase in the  $L_y$  for turbulent conditions within the cavity however these eddies remain smaller than the laminar condition. However,  $L_x$  does experience a minor increase upon interacting with the ramp, indicating the importance of the shear layer reattachment region and its influence on the vorticity generated within the combustor. This indicates that after the shear layer reattaches and flow exits the cavity there is an introduction of larger vortex structures into the flow-field and turbulence ex-



**Fig. 9.** Average vorticity ( $\omega_z$ ) with streamlines overlaid. Gray line indicates  $v_x = 0$  m/s band to identify shear layer reattachment.

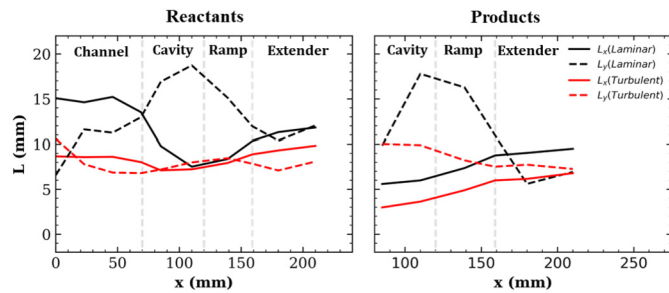


**Fig. 10.** Integral length scales  $L_x$  and  $L_y$  for reactants and products as function of  $x$  location for reacting laminar and turbulent inflow conditions.

perienced from the freestream. Examining the length scales within the product region reveal that  $L_x$  is smaller than the reactants for the laminar inflow configuration. For the turbulent inflow condition both  $L_x$  and  $L_y$  are slightly smaller than the reactant scales. This indicates that the heat release of combustion has a minor impact on the integral length scales within the flow in contrast to the Kolmogorov scales.

The turbulent energy spectra are also a key metric for understanding the distribution of turbulent energy-containing eddies within the flowfield. The turbulent energy spectra, sampled at

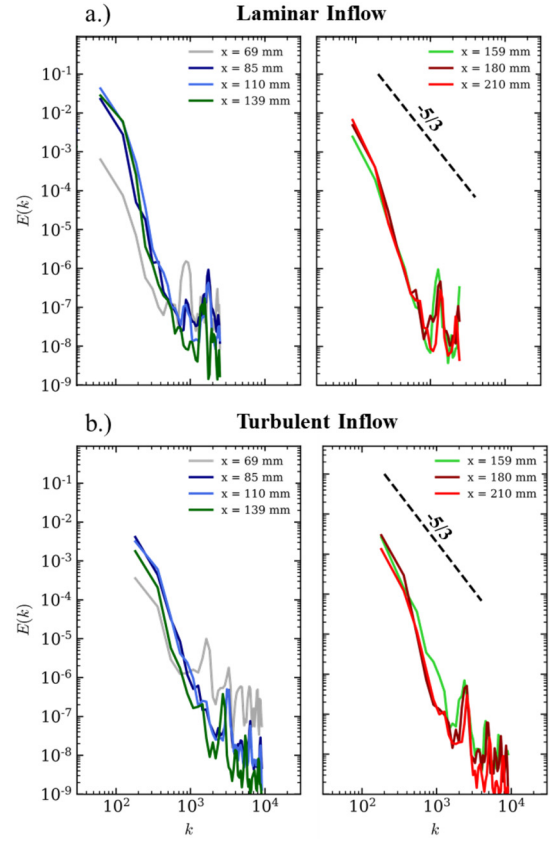


**Fig. 11.** Turbulent energy spectra as a function of  $x$  location for a.) laminar and b.) turbulent inflow conditions.

the same locations as the integral length scales are presented in Fig. 11. The spectra from each condition span a different wavenumber range corresponding to the integral length scales down to the Kolmogorov scales for the laminar inflow or the resolution limit for the turbulent inflow. The results indicate that the energy is primarily driven by large scale eddies within the cavity ( $x = 85, 110$  mm) for both inflow conditions due to the vorticity shedding within the shear layer. In the laminar inflow case, the energy within the flowfield diminishes in the streamwise direction as the large scale vortices shed in the cavity shear layer dissipate and there is minimal turbulent kinetic energy retained in the flow.

However, in the turbulent inflow case where there is turbulent kinetic energy applied to the flow due initially due to the incoming turbulence, the energy within the remains nominally constant for the large energy containing eddies throughout the domain. The primary difference between the inflow boundary conditions is that turbulent inflow results in an increase in energy peaks within the cavity and the start of the ramp. Additionally, there is an increase in the relative amount of the total turbulent kinetic energy contained within the smaller scale vortices for the turbulent inflow condition. The laminar inflow does still have small scale energy-containing eddies but to a lesser degree, indicating that the cavity and ramp have a strong influence on the flame-vortex interactions which occur within the combustor.

### 3.1.4. Instantaneous results

To visualize how the changing length scales and turbulent kinetic energy distributions influence the flame and flow field, instantaneous vorticity contours with the flame location overlaid are provided in Fig. 12. The results indicate that the primary source of vorticity generation under laminar conditions comes from the shedding of large eddies from the cavity lip. These large scale eddies result in broad wrinkling of the flame surface, which prop-

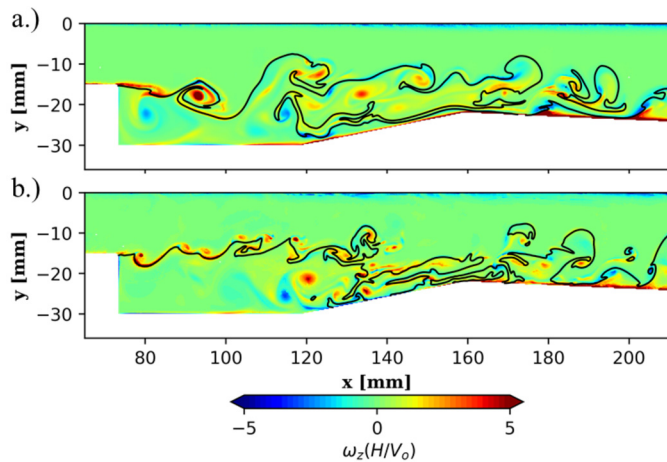


**Fig. 12.** Instantaneous vorticity contours with flame overlaid for a.) laminar and b.) turbulent inflow.

agates and persists downstream. In contrast, under higher turbulence conditions, eddies shed from the cavity are smaller and occur at faster rate, resulting in increased small scale wrinkling of the flame surface. It is notable that vortices are present within the products, near the base of the ramp, as a result of the shear layer reattaching on the cavity aft wall. These eddies have a higher magnitude of vorticity under turbulent inflow conditions, as a result of the stronger recirculation region. This result corresponds with the results depicted in Fig. 10, which illustrates an increase in length scales within the ramp region of the combustor. The primary difference on the ramp is the noticeable amount of smaller eddies occurring under turbulent conditions, which corresponds to the energy spectra distributions in Fig. 11.

With the understanding that flame-vortex interactions are a significant form of instability that exist within many combustion facilities, the vorticity and flame are examined through time to gain insight into the dynamics occurring within the combustor [13,19]. There is an instability which occurs within the cavity where there is a buildup of vorticity from the shear layer and ramp which results in a break in the cohesive flame structure. An example of this behavior is depicted within Fig. 13, which shows instantaneous temperature and vorticity contours at 0.05 millisecond intervals. The sequence occurs as strong eddies generated from the cavity lip begin to pull low temperature reactants into the cavity. As the eddies proceed lower into the cavity they interact with the recirculation region and strong negative stream-wise velocity which allows them to remain stationary within the cavity between frames 3 and 4. At this point the vorticity within the cavity reaches a maximum, while the temperature reaches a minimum as the ramp is filled with reactants. The large eddy which initiated the instability is then recirculated back to the shear layer where it is expelled downstream, carrying with it the high temperature combustion products which remained trapped near the cavity lip. This oscillatory behavior between the vorticity and temperature occurs throughout the simulation for both laminar and turbulent inflow. While this instability does not prevent the flame from stabilizing in the shear layer, it does periodically allow for a low temperature pocket to enter the cavity and not undergoes a reaction. The cavity shear layer remains ignited as the instability creates an environment where the eddies from the shear layer trap the combustion products near the wall, where they are held in the small recirculation zone generated by the secondary vortex visualized in Fig. 9.

Combustion instabilities are often characterized by flow oscillations and pressure fluctuations [13]. Pressure fluctuations extracted from the cavity region (73–118 mm) of the combustor and presented in Fig. 14 for both laminar and turbulent inflow conditions.

High magnitude fluctuations are present for both conditions, however there are smaller scale fluctuations which occur at a higher frequency for the turbulent inflow condition. The laminar pressure fluctuation reach a similar peak each cycle, however the turbulent inflow condition contains different magnitude peak fluctuations throughout. This indicates that the unsteady turbulent fluctuations generate non-uniform oscillatory behavior within the cavity. By quantifying the time between peaks for each inflow condition, it is determined that the average laminar time scale ( $t_L$ ) is approximately 2 ms and the turbulent time scale ( $t_T$ ) is approximately 1.4 ms. This shift to higher frequency oscillatory mode driven by the turbulence is important to note as different engine operating conditions can result in increasing instability and inhibit performance.

To further explore the cause of the instability witnessed in Fig. 13, a frequency analysis is performed on the vorticity in the cavity shear layer and ramp. The analysis is performed by extracting the temporal vorticity signal within the cavity shear layer and in the region near the cavity ramp below where the shear layer reattaches. The frequency analysis is then performed utilizing Welch's overlapping segment method [44]. The results for both the laminar and turbulent inflow are presented in Fig. 15. It is notable that the vorticity shed from the shear layer is shed at a very similar rate to that of the ramp under each inflow condition. Additionally, under laminar conditions there is a sharp decrease from low to high frequency which is not present under turbulent inflow conditions indicating a faster, less uniform shedding rate. This non-uniform shedding rate coincides the findings in Fig. 14 which shows non uniform peaks in the pressure fluctuation which could be a function of the shedding frequency. The laminar inflow condition is dominated by low frequency shedding which corresponds well with the uniform peaks and distribution.

Comparing the peak frequencies with that of the time captured between the pressure oscillations determined in Fig. 14, it is seen that the times  $t_L$  and  $t_T$  correspond well to the first peak of the ramp vortex shedding for each condition. This indicates that there is a link between the vorticity shed from the ramp at the shear layer reattachment region and the pressure oscillations which drive the combustion instability presented in Fig. 13. The dynamics of the vorticity shed from the ramp due to the shear layer reattachment can have a significant impact on the dynamics which occur within the cavity. However, since the behavior is driven by the ramp it does not affect the cavity shear layer region which remains filled with high temperature combustion products ensuring a sustained reaction despite high magnitude pressure fluctuations.

### 3.2. Three-dimensional simulation

A three-dimensional simulation was performed to capture any out of plane effects not captured by the two-dimensional simulation. The simulation is performed with the same boundary conditions as the two-dimensional case and by extending the domain 10 mm in the z-direction. The edges of domain ( $z = 0$  and 10 mm) are defined using periodic boundary conditions. The 3D simulation is completed only for the turbulent inflow boundary condition. A coarser 300  $\mu\text{m}$  element mesh is utilized in the core flow to limit the computational expense. The mesh is refined in the cavity shear layer and downstream of the ramp with an element size of 140  $\mu\text{m}$  and 200  $\mu\text{m}$  in each region, respectively. This resulted in a total of approximately 9 million tetrahedral elements in the 3D mesh.

Average contours of the time-averaged CO mass fraction at  $z = 3$  mm and  $z = 7$  mm in Fig. 16a and 16b to identify the flame angle of three-dimensional simulation. It is noted, that the flame angle in the three-dimensional simulation does increase and matches more closely with the anticipated angle using the Peters correlation. Instantaneous isosurfaces of temperature at 1500,



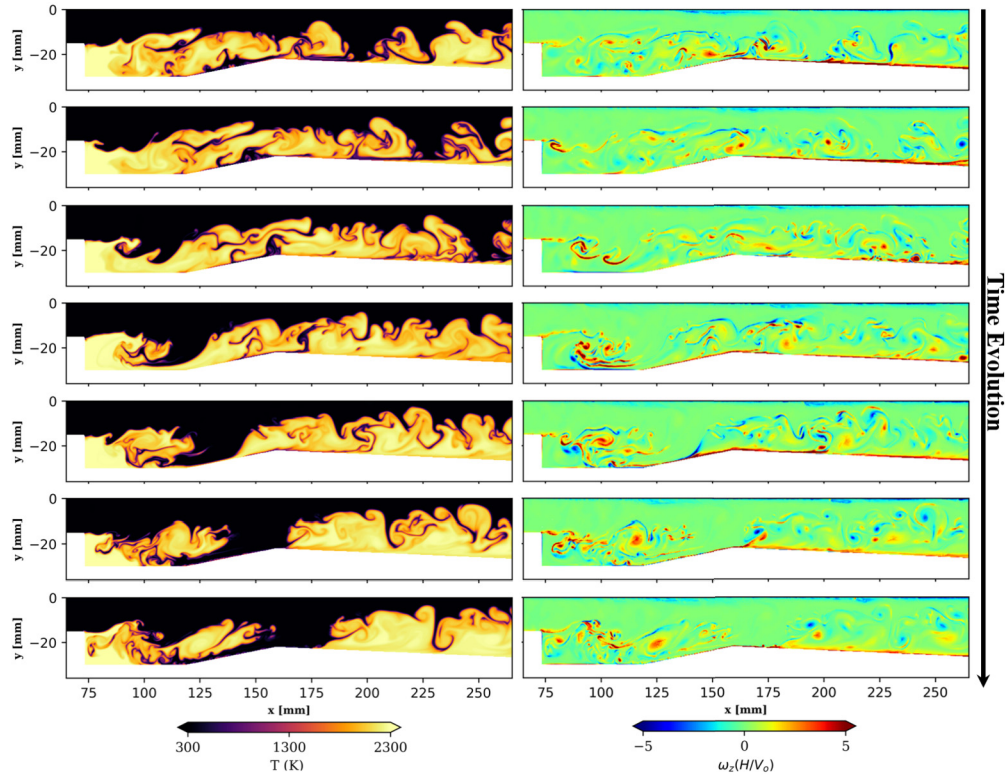


**Fig. 13.** Instantaneous contours of temperature and vorticity for the turbulent inflow conditions illustrating vorticity driven flame instability. Images are separated 0.05 ms.

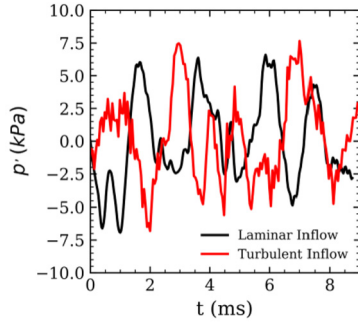


**Fig. 14.** Pressure fluctuations within the cavity for the laminar and turbulent inflow conditions.

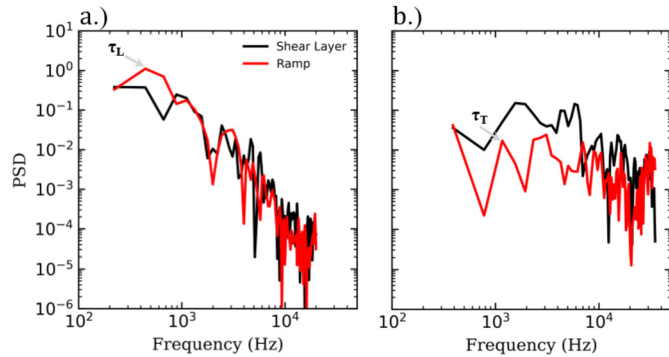


**Fig. 15.** PSD of vorticity of from the shear layer and ramp for a.) laminar and b.) turbulent inflow.

1700, 1900 K are used to identify the flame and colored by the normalized spanwise vorticity ( $\omega_z(H/V_0)$ ) is presented in Fig. 16 to visualize the flame-vortex interactions. Similarly to the two-dimensional simulations, there is strong vorticity production in

the shear layer of the cavity, primarily in the region where the flame attaches. This vorticity dissipates downstream until the ramp where the shear layer reattaches. It is noted that after reattachment the spanwise vorticity shifts to a primarily negative distribution and increased flame rollup occurs. Additionally, the flame rollup occurs at an increased frequency after interaction with the ramp, further exemplifying the impact the ramp has on the flame-vortex interactions.

To identify any three dimensional impacts on the vorticity dynamics further, average contours of vorticity ( $\omega_z$ ) with streamlines are presented in Fig. 17 at the midplane ( $z = 5$  mm) and 4 mm offset from the mid-plane. The results indicate very similar flow-features in the  $z$ -domain with the shear layer reattaching at  $x = 132$  mm for each plane. This is an approximately 6 mm decrease from the two dimensional simulation which reattached at 138 mm. A noticeable difference between the two and three dimensional simulations is the size of the secondary vortex generated near the cavity lip. Under the turbulent inflow in the two-dimensional case, the secondary vortex was heavily suppressed by the primary vortex generated off the ramp. However, in the three-dimensional case the size of the secondary vortex is approximately 16 mm compared to 10 mm in the two-dimensional case.

Similarly to the two-dimensional simulations, the integral length scales are calculated at the cavity lip ( $x = 69$  mm) prior to the flame and at the end of the ramp ( $x = 159$  mm). The results are presented in Table 3 for both locations. It is noted that when compared to the two dimensional simulation the length scales  $L_x$  and  $L_y$  are approximately 1 mm larger at the cavity lip and 3 mm larger at the ramp inflection point.

Additionally, the turbulent energy spectra are computed at these two locations to examine if the addition of span-wise velocity fluctuations alters the results to a significant degree. The spectra are shown in Fig. 18 and at the cavity lip it is noted that the spectra decay more closely to the  $-5/3$  slope spectrum than the two-dimensional spectra shown in Fig. 11. It is once again demon-



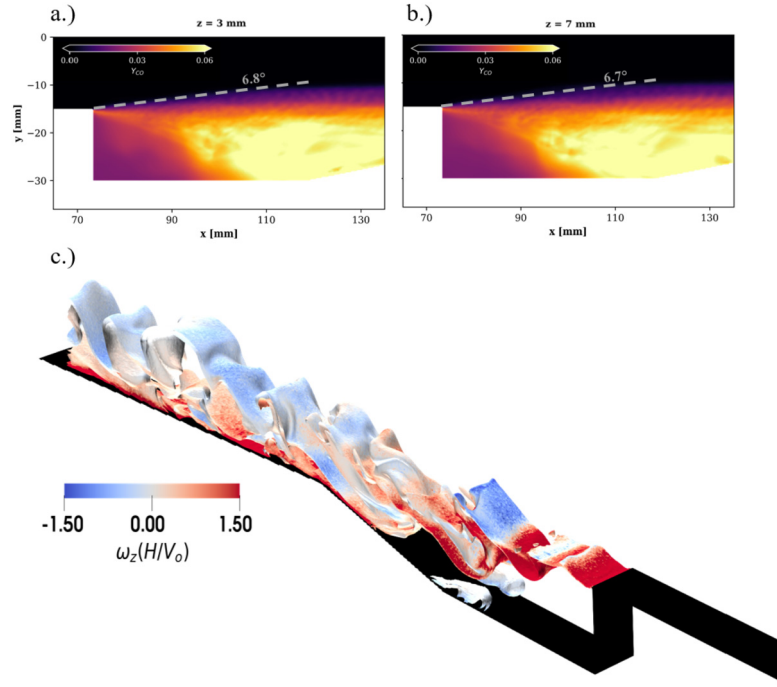


**Fig. 16.** Time averaged CO mass fraction at a.)  $z = 3$  mm and b.)  $z = 7$  mm. c.) Instantaneous isosurfaces of  $T = 1500, 1700, 1900$  K colored by normalized spanwise vorticity ( $\omega_z(H/V_o)$ ).

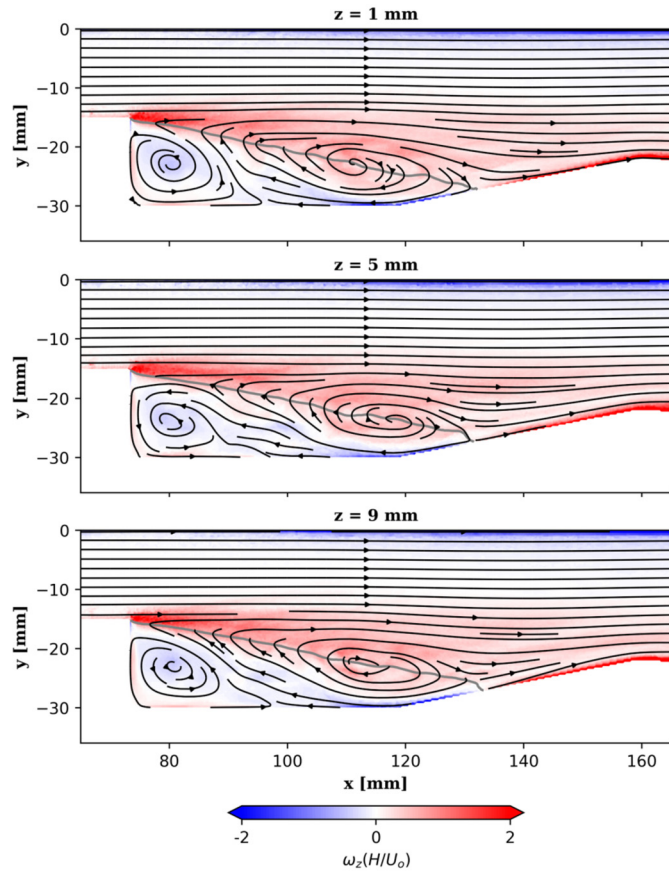


**Fig. 17.** Average vorticity ( $\omega_z$ ) at  $z = 1$  mm,  $z = 5$  mm, and  $z = 9$  mm with streamlines overlaid. Gray line indicates  $v_x = 0$  m/s band to identify shear layer reattachment.

**Table 3**

Calculated Length Scales for 3D Simulation.

Location	$L_x$ (mm)	$L_y$ (mm)	$L_z$ (mm)
Cavity Lip (69 mm)	10.3	9.43	9.81
Ramp (159 mm Reactants)	15.18	13.61	14.08
Ramp (159 mm Products)	14.25	13.95	13.09

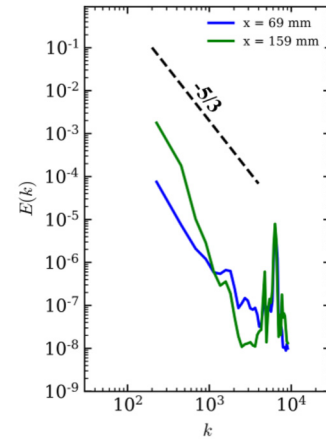


**Fig. 18.** Turbulent energy spectra at the cavity lip ( $x = 69$  mm) and the end of the ramp ( $x = 159$  mm).

stated that at the ramp there is an increase in the amount of small scale turbulent eddies contributing to turbulent kinetic energy production within the cavity. To examine the impact of the flame-vortex interaction in three dimensions, the pressure oscillations are extracted from the three-dimensional simulation center-plane and presented in Fig. 19. Similar oscillatory behavior is experienced, however, compared to the two-dimensional simulation, there is an increase in the time between peaks to approximately 1.9 ms. The decrease in pressure oscillations within the cavity can be attributed to the larger secondary vortex formation within the cavity. Hong et al. determined that as the secondary vortex became fur-

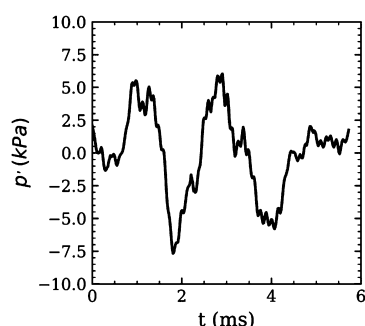


Fig. 19. Pressure fluctuations within the cavity for the three-dimensional simulation.

ther suppressed there is a transition within the combustor towards thermoacoustic instability [11]. This indicates that the instability is still present, however, at a lower frequency as the turbulence-flame interactions are spread across the entirety of the three-dimensional domain.

#### 4. Conclusions

Numerical simulations of premixed ethylene-air cavity stabilized flames were performed utilizing laminar and turbulent inflow boundary conditions to isolate the impact of augmented turbulence on the flame and flow field. A three step, seven species chemical mechanism was utilized to simulate the stoichiometric ethylene-air combustion. The simulations were compared to experimental PIV and chemiluminescence measurements to confirm that the inflow conditions and flame behavior are adequately captured by the simulation.

The two-dimensional simulations demonstrated that there are primary and secondary vortices which form within the cavity recirculation region. Utilizing the turbulent inflow conditions it is demonstrated that the primary vortex is enlarged and is coupled with a decrease in the shear layer reattachment length. The integral length scales are examined at discrete locations throughout the flow field to identify the evolution throughout the domain. The laminar inflow boundary condition results in larger integral length scales occurring within the cavity region as larger eddies are shed from the cavity lip, while the turbulent inflow experiences relatively constant smaller integral scales. Similarly, the turbulent energy spectra are calculated for each inflow condition and it is noted that the energy containing eddies within the flow begins to shift towards smaller structures at the aft wall region. Instantaneous contours of the vorticity and the flame structure confirmed these findings, as the turbulent inflow simulation experiences smaller scale wrinkling of the flame front and an increase in small turbulent eddies forming in the shear layer reattachment region.

Further examining the interaction between the flame and vorticity field reveals oscillatory behavior occurring within the cavity. A flame-vortex interaction driven instability is generated by eddies shed from the shear layer pulling an increased amount of low temperature reactants into the cavity. The eddies do not propagate downstream but instead remain stationary in the cavity creating a break in the cohesive structure of the flame. This oscillatory behavior of the vorticity and temperature within the cavity is analyzed further by quantifying the pressure fluctuations within the combustor. It is demonstrated that under high turbulence conditions, the instability shifts to a higher frequency mode. This shift can be attributed to the suppression of the secondary vortex which has been shown to be indicative of thermoacoustic instabilities within combustors. The frequency of the pressure oscillations correlates well with the peak in the shedding frequency of vorticity from the ramp, revealing that the shear layer reattachment region is

a significant contributor to the flame-vortex interaction instability within this flameholder configuration.

A three-dimensional simulation was performed utilizing the turbulent inflow boundary condition to calculate the same statistics calculated in the two-dimensional case to examine any three-dimensional effects. It is shown that the three-dimensional simulation captures the flame angle more closely to theoretical calculations. The results for the integral length scales and turbulent energy spectra revealed the same trends however, the length scales were slightly smaller for the two-dimensional simulations. The pressure oscillations are captured in the three-dimensional case as well and reveal similar trends, although occurring at a lower frequency. This indicates that under these turbulence conditions, the statistics measured from the two-dimensional simulation provide adequate insight into the flow behaviors within the cavity.

#### Declaration of competing interest

The authors declare that they have no known competing financial interests or personal relationships that could have appeared to influence the work reported in this paper.

#### Acknowledgements

The authors would like to acknowledge the support of the Base Program at the Naval Research Laboratory.

#### References

- [1] A. Ben-Yakar, R.K. Hanson, Cavity flame-holders for ignition and flame stabilization in scramjets: an overview, *J. Propuls. Power* 17 (4) (2001) 869–877.
- [2] M. Gruber, R. Baurle, T. Mathur, K.Y. Hsu, Fundamental studies of cavity-based flameholder concepts for supersonic combustors, *J. Propuls. Power* 17 (1) (2001) 146–153.
- [3] C.C. Rasmussen, J.F. Driscoll, K.Y. Hsu, J.M. Donbar, M.R. Gruber, C.D. Carter, Stability limits of cavity-stabilized flames in supersonic flow, *Proc. Combust. Inst.* 30 (2) (2005) 2825–2833.
- [4] L. Huellmantel, R. Ziemer, A.B. Cambel, Stabilization of premixed propane-air flames in recessed ducts, *J. Jet Propul.* 27 (1) (1957) 31–34.
- [5] G. Winterfeld, On processes of turbulent exchange behind flame holders, *Symp., Int., Combust.* 10 (1) (1965) 1265–1275.
- [6] W. Humphries, J. Vincent, Near wake properties of axisymmetric bluff body flows, *Appl. Sci. Res.* 32 (6) (1976) 649–669.
- [7] J. Pan, M. Vangsness, D. Ballal, Aerodynamics of bluff-body stabilized confined turbulent premixed flames, *J. Eng. Gas Turbines Power* 114 (4) (1992) 783–789.
- [8] J.C. Massey, I. Langella, N. Swaminathan, A scaling law for the recirculation zone length behind a bluff body in reacting flows, *J. Fluid Mech.* 875 (2019) 699–724.
- [9] R.D. Gould, W.H. Stevenson, H.D. Thompson, Simultaneous velocity and temperature measurements in a premixed dump combustor, *J. Propuls. Power* 10 (5) (1994) 639–645.
- [10] R.S. Gabruk, L.A. Roe, Velocity characteristics of reacting and nonreacting flows in a dump combustor, *J. Propuls. Power* 10 (2) (1994) 148–154.
- [11] S. Hong, S.J. Shanbhogue, A.F. Ghoniem, Impact of fuel composition on the recirculation zone structure and its role in lean premixed flame anchoring, *Proc. Combust. Inst.* 35 (2) (2015) 1493–1500.
- [12] P.H. Renard, D. Thévenin, J. Rolon, S. Candel, Dynamics of flame/vortex interactions, *Prog. Energy Combust. Sci.* 26 (3) (2000) 225–282.
- [13] H.M. Altay, R.L. Speth, D.E. Hudgins, A.F. Ghoniem, Flame-vortex interaction driven combustion dynamics in a backward-facing step combustor, *Combust. Flame* 156 (5) (2009) 1111–1125.
- [14] J.M. Samaniego, T. Mantel, Fundamental mechanisms in premixed turbulent flame propagation via flame-vortex interactions: part I: experiment, *Combust. Flame* 118 (4) (1999) 537–556.
- [15] K. Ahn, H.Y. Kenneth, Effects of damköhler number on vortex-flame interaction, *Combust. Flame* 159 (2) (2012) 686–696.
- [16] H.Y. Ken, A. Trouvé, J.W. Daily, Low-frequency pressure oscillations in a model ramjet combustor, *J. Fluid Mech.* 232 (1991) 47–72.
- [17] T.J. Poinsot, A.C. Trouve, D.P. Veynante, S.M. Candel, E.J. Esposito, Vortex-driven acoustically coupled combustion instabilities, *J. Fluid Mech.* 177 (1987) 265–292.
- [18] K.I. Matveev, F. Culick, A model for combustion instability involving vortex shedding, *Combust. Sci. Technol.* 175 (6) (2003) 1059–1083.

- [19] A.F. Ghoniem, S. Park, A. Wachsman, A. Annaswamy, D. Wee, H.M. Altay, Mechanism of combustion dynamics in a backward-facing step stabilized premixed flame, *Proc. Combust. Inst.* 30 (2) (2005) 1783–1790.
- [20] N. Peters, *Turbulent Combustion*, Cambridge University Press, 2000.
- [21] P.E. Hamlington, A.Y. Poludnenko, E.S. Oran, Intermittency in premixed turbulent reacting flows, *Phys. Fluids* 24 (7) (2012) 075,111.
- [22] P.E. Hamlington, A.Y. Poludnenko, E.S. Oran, Interactions between turbulence and flames in premixed reacting flows, *Phys. Fluids* 23 (12) (2011) 125,111.
- [23] N. Chakraborty, Statistics of vorticity alignment with local strain rates in turbulent premixed flames, *Eur. J. Mech. B, Fluids* 46 (2014) 201–220.
- [24] A.N. Lipatnikov, S. Nishiki, T. Hasegawa, A direct numerical simulation study of vorticity transformation in weakly turbulent premixed flames, *Phys. Fluids* 26 (10) (2014) 105,104.
- [25] B. Bobbitt, S. Lapointe, G. Blanquart, Vorticity transformation in high Karlovitz number premixed flames, *Phys. Fluids* 28 (1) (2016) 015,101.
- [26] G. Damkohler, Der einfluss der turbulenz auf die flammengeschwindigkeit in gasgemischen, *Z. Elektrochem. Angew. Phys. Chem.* 46 (11) (1940) 601–626.
- [27] A.W. Skiba, C.D. Carter, S.D. Hammack, J.D. Miller, J.R. Gord, J.F. Driscoll, The influence of large eddies on the structure of turbulent premixed flames characterized with stereo-piv and multi-species plif at 20 khz, *Proc. Combust. Inst.* 37 (2) (2019) 2477–2484.
- [28] R.F. Johnson, A.D. Kercher, A conservative discontinuous Galerkin discretization for the chemically reacting Navier-Stokes equations, *J. Comput. Phys.* 423 (2020) 109,826.
- [29] S. Gottlieb, C.W. Shu, E. Tadmor, Strong stability-preserving high-order time discretization methods, *SIAM Rev.* 43 (1) (2001) 89–112.
- [30] E. Hassan, D.M. Peterson, D.K. Walters, E.A. Luke, Dynamic hybrid Reynolds-averaged Navier–Stokes/large-Eddy simulation of a supersonic cavity: chemistry effects, *J. Propuls. Power* 35 (1) (2019) 201–212.
- [31] D.M. Peterson, High-resolution simulations of premixed combustion in a supersonic cavity, in: *AIAA Scitech 2019 Forum*, 2019, p. 0448.
- [32] S.B. Pope, *Turbulent Flows*, Cambridge University Press, 2000.
- [33] L. Davidson, Using isotropic synthetic fluctuations as inlet boundary conditions for unsteady simulations, *Adv. Appl. Fluid Mech.* (2007) 1–35.
- [34] S. Buhl, F. Gleiss, M. Köhler, F. Hartmann, D. Messig, C. Brückner, C. Hasse, A combined numerical and experimental study of the 3d tumble structure and piston boundary layer development during the intake stroke of a gasoline engine, *Flow Turbul. Combust.* 98 (2) (2017) 579–600.
- [35] S. Gallier, M. Plaud, A model for solid propellant burning fluctuations using mesoscale simulations, *Acta Astronaut.* 158 (2019) 296–303.
- [36] G.B. Goodwin, C.L. Bachman, R.F. Johnson, D.A. Kessler, Synthetic Freestream Turbulence Generation at an Inflow Boundary Condition, in: *AIAA Scitech 2021 Forum*, 2021, p. 1846.
- [37] G.B. Goodwin, R.F. Johnson, D. Kessler, H.K. Chelliah, Premixed ethylene-air combustion in a dual-mode scramjet cavity combustor with a turbulent inflow, in: *AIAA Propulsion and Energy 2019 Forum*, 2019, p. 4270.
- [38] T.B. Nielsen, J.R. Edwards, H.K. Chelliah, D. Lieber, C. Geipel, C.P. Goynes, R.D. Rockwell, A.D. Cutler, Hybrid large Eddy simulation/Reynolds-averaged Navier–Stokes analysis of a premixed ethylene-fueled dual-mode scramjet combustor, *AIAA J.* 59 (7) (2021) 2440–2456.
- [39] P.A. Davidson, *Turbulence: An Introduction for Scientists and Engineers*, Oxford University Press, 2015.
- [40] A.H. Rauch, H.K. Chelliah, On the ambiguity of premixed flame thickness definition of highly pre-heated mixtures and its implication on turbulent combustion regimes, *Combust. Theory Model.* 24 (4) (2020) 573–588.
- [41] A.J. Morales, I.M. Lasky, M.K. Geikie, C.A. Engelmann, K.A. Ahmed, Mechanisms of flame extinction and lean blowout of bluff body stabilized flames, *Combust. Flame* 203 (2019) 31–45.
- [42] M.K. Geikie, C.J. Rising, A.J. Morales, K.A. Ahmed, Turbulent flame-vortex dynamics of bluff-body premixed flames, *Combust. Flame* 223 (2021) 28–41.
- [43] N. Peters, The turbulent burning velocity for large-scale and small-scale turbulence, *J. Fluid Mech.* 384 (1999) 107–132.
- [44] P. Welch, The use of fast Fourier transform for the estimation of power spectra: a method based on time averaging over short, modified periodograms, *IEEE Trans. Audio Electroacoust.* 15 (2) (1967) 70–73.